Insights into Titan's geology and hydrology based on enhanced image processing of Cassini RADAR data

Antoine Lucas, Oded Aharonson, Charles-Alban Deledalle, Alexander G. Hayes, Randolph Kirk, Elpitha Howington-Kraus

HAL Id: hal-01072249

https://hal.science/hal-01072249

Insights into Titan's geology and hydrology based on enhanced image processing of Cassini RADAR data

Antoine Lucas[1,2], Oded Aharonson[1,3], Charles Deledalle[4,5], Alexander G. Hayes[1,6], Randolph Kirk[7], and Elpitha Howington-Kraus[7]

[1] Division of Geological and Planetary Sciences, California Institute of Technology, Pasadena, California, USA, [2] Laboratoire Astrophysique, Instrumentation et Modélisation, CNRS-UMR 7158, Paris VII–Denis Diderot University–CEA-SACLAY, Gif-sur-Yvette, France, [3] Weizmann Institute of Science, Center for Planetary Science, Rehovot, Israel, [4] Telecom, Paris-Tech, CNRS LTCI, Paris, France, [5] Institut de Mathématiques de Bordeaux, Bordeaux, France, [6] Spacecraft Planetary Imaging Facility, Cornell University, Ithaca, New York, USA, [7] Astrogeology Branch, USGS, Flagstaff, Arizona, USA

Abstract The Cassini Synthetic Aperture Radar has been acquiring images of Titan's surface since October 2004. To date, 59% of Titan's surface has been imaged by radar, with significant regions imaged more than once. Radar data suffer from speckle noise hindering interpretation of small-scale features and comparison of reimaged regions for change detection. We present here a new image analysis technique that combines a denoising algorithm with mapping and quantitative measurements that greatly enhance the utility of the data and offers previously unattainable insights. After validating the technique, we demonstrate the potential improvement in understanding of surface processes on Titan and defining global mapping units, focusing on specific landforms including lakes, dunes, mountains, and fluvial features. Lake shorelines are delineated with greater accuracy. Previously unrecognized dissection by fluvial channels emerges beneath shallow methane cover. Dune wavelengths and interdune extents are more precisely measured. A significant refinement in producing digital elevation models is shown. Interactions of fluvial and aeolian processes with topographic relief is more precisely observed and understood than previously. Benches in bathymetry are observed in northern sea Ligeia Mare. Submerged valleys show similar depth suggesting that they are equilibrated with marine benches. These new observations suggest a liquid level increase in the northern sea, which may be due to changes on seasonal or longer timescales.

1. Introduction

The data provided by Cassini-Huygens have been used to identify dune fields, mountains, rivers, and seas [*Elachi et al.*, 2005; *Stofan et al.*, 2006]. As on Earth and ancient Mars, Titan is known to possess an active hydrologic cycle, including lacustrine/marine, fluvial, and pluvial processes [*Stofan et al.*, 2007; *Hayes et al.*, 2008; *Turtle et al.*, 2011]. While isolated small lakes may be fed by atmospheric direct precipitation and sub-surface flow, larger seas with associated channel networks require surface runoff and thus offer analogues to terrestrial drainage systems.

The Cassini RADAR operates in multiple modes: (i) as an imaging SAR (Synthetic Aperture RADAR), (ii) an altimeter, (iii) a radiometer, and (iv) a scatterometer [*Elachi et al.*, 2005]. The imager mode (SAR) provides a spatial sampling up to about 300 m, offering the highest spatial resolution available by Cassini. While operating in SAR mode, the RADAR imaged fluvial networks with tributaries merging and draining into lakes and seas at high latitudes [*Langhans et al.*, 2011; *Burr et al.*, 2012]. While fluvial features have been observed on SAR data with a global distribution, many of them are associated with polar lakes [*Lorenz et al.*, 2008; *Langhans et al.*, 2011; *Burr et al.*, 2012].

The Visual and Infrared Mapping Spectrometer (VIMS) data indicate the presence of specific spectral units accumulated along the borders of some dry/empty lakes south of Ligeia Mare as well as surrounding Ontario Lacus in the southern hemisphere [*Barnes et al.*, 2009], suggesting that evaporation alters the baseline lake level over time. The lake shorelines and associated drainage patterns present an opportunity to observe and understand interactions of fluvial processes with topography on a world with active geologic processes analogous to Earth's.

As of 14 October 2013, up to swath T95, 59% of Titan's surface has been imaged by radar (including SAR and HiSAR modes, 44.5% for SAR only), and ∼25% has been imaged more than once (∼12% excluding data acquired in HiSAR mode). Radar images suffer from speckle noise. This results from random fluctuations caused by coherent processing of the return signal from multiple distributed targets. This multiplicative noise hinders interpretation of small-scale features and comparison of reimaged regions for change detection at the resolution scale [*Goodman*, 1976; *Lee*, 1986; *April and Harvy*, 1991; *Hervet et al.*, 1998; *Schulze and Wu*, 1995; *Polzehl and Spokoiny*, 2006].

We present herein a new processing technique using a nonlocal algorithm for denoising SAR images with an appropriate multiplicative noise model, enabling mapping and quantitative analysis of the images, enhancing the utility of the data, and offering previously unattainable insights on the geology and hydrology of Titan. The denoising technique, tests, and analysis we performed on synthetic images and Cassini RADAR images is described in section 2. We then demonstrate the potential improvement in understanding surface processes on Titan and definition of global mapping units, focusing on specific features including dunes, mountains, and lacustrine terrain. New insights into the geology and hydrology using both SAR and denoised SAR images are provided in section 3, emphasizing the potential of the denoising technique in better understanding Titan's surface. Lake shorelines are delineated with greater accuracy. Previously unrecognized dissection by fluvial channels emerges beneath a shallow hydrocarbons cover, indicating submarine channels. Dune wavelengths and interdune extents are more precisely measured. Interactions of fluvial and aeolian processes with topographic relief is more precisely observed and understood than previously. Furthermore, substantial quantitative improvements are accomplished in computing elevations from radargrammetry. Our enhanced DEM (digital elevation model) allows improved analysis of the topography, with an identification of a clear shoulder in the histogram of elevations, suggesting that fluvial and/or lacustrine processes have affected the distribution by creating a topographic bench in the terrain. Finally, we offer some discussion of Titan's geology and surface processes.

2. Nonlocal Algorithm for Denoising Cassini SAR Images

2.1. Algorithm Description

As stated previously, speckle noise hinders analysis and interpretation of the Cassini SAR images. The noise terms are properties of the surface scatter that are inherent to radar processing. Additionally, additive noise sources are associated with the instrument itself. Instrument noise is here assumed to be negligible as compared to speckle noise. Hence a well-adapted denoising pipeline is valuable. While local filters (moving average filters), Lee filters or Frost filters lead to smoothing (i.e., resolution loss) [*Lee*, 1981; *Frost et al.*, 1982], the nonlocal means (NLM) proposed by *Buades et al.* [2005] efficiently reduce noise and preserve structures. Instead of combining neighboring pixels, the NLM averages pixels in a similar context. NLM assume there are enough redundant pixels (pixels having identical noise-free value) in the image to reduce the noise significantly. An extension of NLM for SAR images has been proposed by *Deledalle et al.* [2009] as described hereafter.

Let $A(x)$ be the observed amplitude at pixel x and $\hat{R}(x)$ its reflectivity. The reflectivity $\hat{R}(x)$ corresponds to the expectation of the square of $A(x)$ over different speckle realizations. The nonlocal estimate of the reflectivity $\hat{R}(x)$ can be obtained using an iterative weighted maximum likelihood estimator as introduced in *Polzehl and Spokoiny* [2006], leading to:

$$\hat{R}^{t+1}(x) = \frac{\sum_{x'} w^{t+1}(x, x') A^2(x')}{\sum_{x'} w^{t+1}(x, x')},$$ (1)

where t is the iteration index, x' is a pixel index belonging to the search window centered on x, whose size is typically $|W| = 21 \times 21$ [*Buades et al.*, 2005], and $w(x, x')$ is a data-driven weight depending on the similarity between pixels with index x and x'.

Pixel similarity can be evaluated by comparing surrounding neighborhoods around x and x' with the use of a criterion based on the joint marginal probability that two noisy regions share an identical underlying value. This leads to the following weight estimator:

$$w^{t+1}(x, x') = \exp\left[-\frac{1}{h^2} \sum_{\tau} \log\left(\frac{A(x+\tau)}{A(x'+\tau)} + \frac{A(x'+\tau)}{A(x+\tau)}\right) - \frac{1}{T} \sum_{\tau} \frac{(\hat{R}^t(x+\tau) - \hat{R}^t(x'+\tau))^2}{\hat{R}^t(x+\tau)\hat{R}^t(x'+\tau)}\right],$$ (2)

where τ is a relative displacement vector such that $x + \tau$ and $x' + \tau$ spanned the pixels of the neighborhoods of x and x', respectively (i.e., these similarity windows are typically of size $|\Delta| = 7 \times 7$), and h^2 and T are two filtering parameters used to balance the trade-off between the noise reduction and the estimation fidelity. While h^2 controls the fidelity to the noisy amplitudes and hence acts on the noise reduction level, T controls the fidelity to the preestimation $\hat{R}^t$ obtained at the previous iteration. Discussion on relative effects of these parameters can be found in *Polzehl and Spokoiny* [2006] and *Deledalle et al.* [2009], specific examples are given in Text S1 in the supporting information.

SAR images are commonly considered to be corrupted by a multiplicative noise with either a Rayleigh distribution (for amplitude images) or an exponential distribution (for intensity images) [*Goodman*, 1976; *Hervet et al.*, 1998; *Schulze and Wu*, 1995]. Multilook SAR images are expected to follow a gamma distribution according to *Lee* [1986] and *April and Harvy* [1991]. We consider these noise distributions in the analysis below and demonstrate the robustness of the technique against various distributions. Although in Cassini SAR data the number of looks varies along the swath, the current algorithm is designed for single looks [see *Deledalle et al.*, 2009] but efforts to quantify the effects of variable numbers of looks are discussed in Text S1.

2.2. Synthetic Tests

In order to evaluate the utility and fidelity of the denoising process, we tested various distributions of multiplicative noise on a synthetic image. The synthetic image is a periodic signal (sine function) with an exponential decay in amplitude in both directions, so as to obtain a varying signal to noise ratio in the image. Three noise models were tested with exponential, Rayleigh, and gamma distributions (i.e., for the gamma distribution, we used three as a typical value for the number of looks, unless specified).

Figure 1a illustrates our various tests and shows how the different distributions of noise affect the synthetic image. Visual inspection reveals the denoised image resembles the original (noise-free) image in qualitative appearance: structures observed in the noise-free image for the three types of noise distributions are retrieved in the denoised image. Structures obscured by speckle noise can be retrieved with the denoising process (i.e., the brightness contrasts and oscillations from the original noise-free image are recovered).

Quantitatively, the probability distribution function (PDF) of the noise distribution removed has the same characteristics (mean and variance) as the noise initially introduced, without providing any prior information on noise characteristics, for all three tested noise distributions (see Figure 1b). The noise distributions that were removed had RMS values that were close to the RMS of the introduced distributions; the RMS values differed by −7%, −2%, and 4%, for the exponential, Rayleigh, and gamma distributions, respectively.

Cross sections along the diagonal (Figure 1a) illustrate the accuracy of the denoising process in retrieving the original noise-free brightness amplitude and structures. Oscillations from the noise-free image are correctly retrieved after denoising in all tested noise distributions. Specifically, when compared to the known original image, the variance of the residual of the denoised images are 2 orders of magnitude smaller than the noisy images. Comparable results are obtained for all three noise distributions that were tested. This shows that without providing a prior assumption on the noise distribution, the technique is able to remove noise and that the removed component has characteristics similar to the noise effectively present in the signal over a wide range of noise characteristics. Figure 2 illustrates a more complex case but show similar performances of the techniques (see also Text S1 for further tests).

2.3. Application to Cassini SAR Images

The synthetic tests guide the optimization of the choice of adaptive denoising parameters and apply the algorithm to the Cassini Radar SAR images. Evaluated ranges for the parameters are $h^2 \in [1; 15]$, $T \in [1; 15]$, $t \in [1; 4]$, $|W| \in [11 \times 11; 41 \times 41]$, and $|\Delta| \in [5 \times 5; 11 \times 11]$. We introduce a denoised data set we call NLDSAR (Nonlocal Denoised SAR) hereafter. Figure 3 shows three regions with different morphological characteristics (mountainous region, large sea shorelines, and dune field) from swaths T17 and T28. Our tests show that these three regions have different characteristics, described below.

Figure 3a shows that the removed multiplicative noise in this mountainous region resembles a Rayleigh (or gamma) distribution with an RMS of 0.933. Edges of mountains are preserved but plains appear smoother compared to the noisy SAR image. The noise distribution in the lake area (Figure 3b) is similar to the previous case with an RMS of 1.106. When examining the image, shorelines are better defined and easier to identify. The unimodal distribution of the backscatter values over the dune field (Figure 3c) indicates that slopes of each of the dune faces varies gradually (in contrast to, for example, a bimodal distribution) indicating a
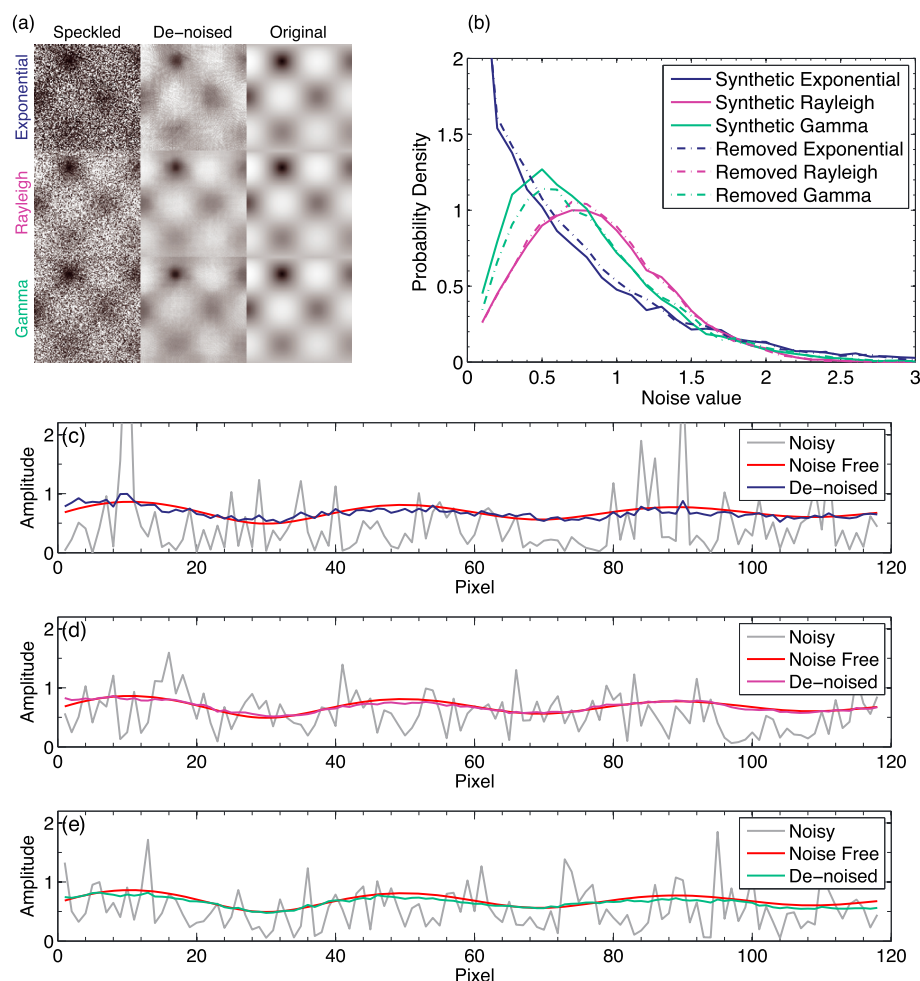
Figure 1. (a) Synthetic tests of denoising image affected by multiplicative noise, respectively, with exponential, Rayleigh, and gamma distributions. (b) Distribution functions of the synthetic exponential, Rayleigh, and gamma noises and their removed counterparts. Cross sections along diagonal (upper left, lower right) of images of synthetic tests for (c) exponential noise, (d) Rayleigh noise, and (e) gamma noise.

varying slope on each face of the dune. The noise distribution is different from the previous two examples with a larger fraction of low noise values. The removed noise distribution RMS is 0.972. As dune morphogenesis can be investigated from statistical analysis of crest orientation, connectivity, spacing, and length [*Kocurek and Ewing*, 2005], studying dune in denoised images is facilitated [*Ewing et al.*, 2013].

Another important aspect of the NLDSAR data is the property that the distribution of the reduced noise is insensitive to the denoising parameters selected (in equation (2)) as shown in Figure 4. When applying the process over a full swath (e.g., swath T17) and varying all of the parameters by 200% the shape of the distribution is only slightly affected but the distribution's characteristics (mean and variance) remain the same. Hence, the NLDSAR data are robust with respect to what may be subjective parameter choices.

To date, the denoising processing has been performed over 28 major segments of SAR swaths using high-performance computing (HPC) facility at Caltech (http://hpc.caltech.edu) and mosaicked together in a global map shown on Figure 5.

3. Geologic Interpretations Using NLDSAR

In addition to geomorphic and mapping analysis improvement, quantitative studies can benefit from NLDSAR products. We present in this section several examples of geologic and hydrologic processes observed at Titan's surface for which we provide new insights enabled by the NLDSAR products.
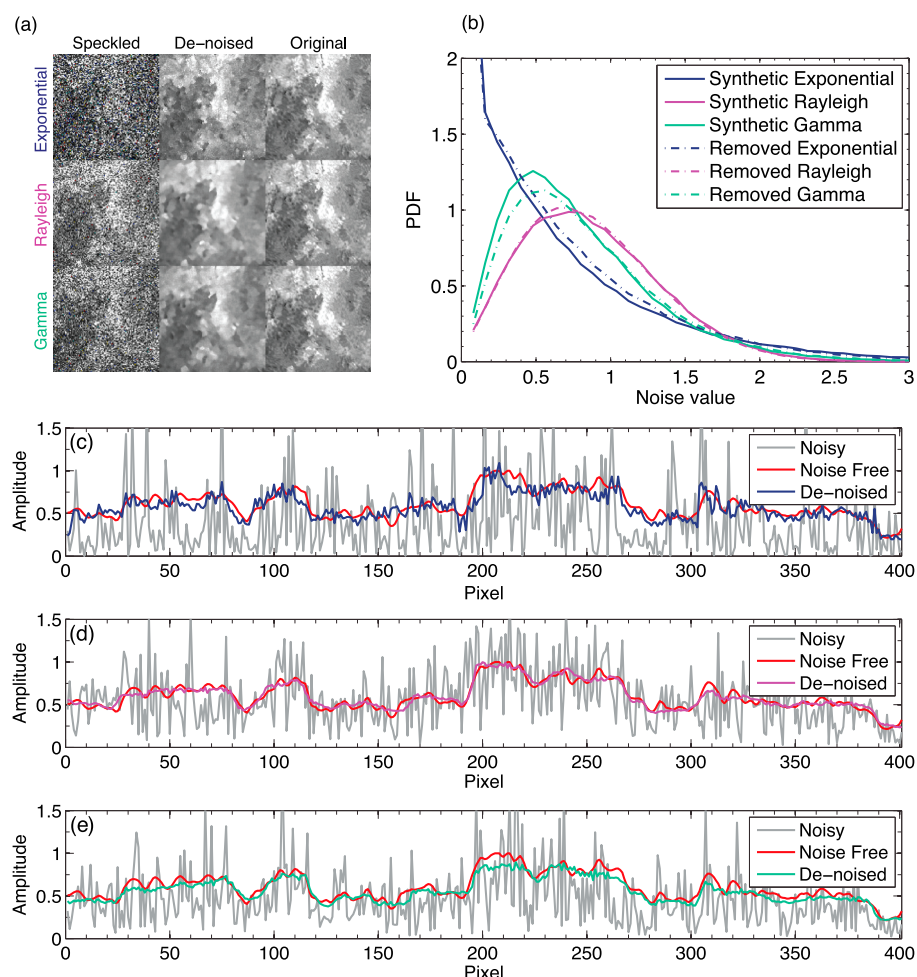
Figure 2. (a) Synthetic tests of denoising image affected by multiplicative noise, respectively, with exponential, Rayleigh, and gamma distributions. The original image is more complex than in Figure 1. (b) Distribution functions of the synthetic exponential, Rayleigh, and gamma noises and their removed counterparts. Cross sections along diagonal (upper left, lower right) of images of synthetic tests for (c) exponential noise, (d) Rayleigh noise, and (e) gamma noise.

3.1. Surface Patchiness

Patches of different brightness are observed in some areas in the NLDSAR data set. In order to consider the origin of these features, we show in Figure 6 the analysis of the patchiness in a region of two overlapping swaths sampling Tortula Facula (8°N, 144°W) with different observation geometries [*Sotin et al.*, 2005]. The western part of the overlap area presents discrete patches of different brightness. As shown, the location, contrast, and morphology of these discrete patches are similar in both NLDSAR images.

The two swaths (T43 and T56) have been acquired in two approximately orthogonal flybys as shown on Figure 6 (see outlines on Titan's sphere). The denoising process is applied with the same parameters (i.e., $h^2 = 6.01$, $T = 0.98$, $|W| = 21 \times 21$, $|\Delta| = 7 \times 7$, and $t = 3$). Incidence angles are 38° and 19° for T43 and T56, respectively. The observation geometries thus differ substantially between these two swaths, providing a useful test case to evaluate the source of the patchiness. We expect that if the patchiness is inherent to Titan's surface, it would be preserved in the two images, while if it is an artificial byproduct of the technique, it would appear to vary in the two very different geometries of observation.

In order to investigate the nature of patches, we performed several tests including synthetic data, SAR data collected on Earth and Venus (see Text S1). We found that varying resolution may affect the appearance of discreet patches. For an Earth image, reducing the spatial resolution to match that of the Cassini SAR, the procedure tends to cluster brightness in discreet ranges to an extent that depends on the trade-off between filter parameters (see Text S1 for detailed tests). We also found that swaths with different
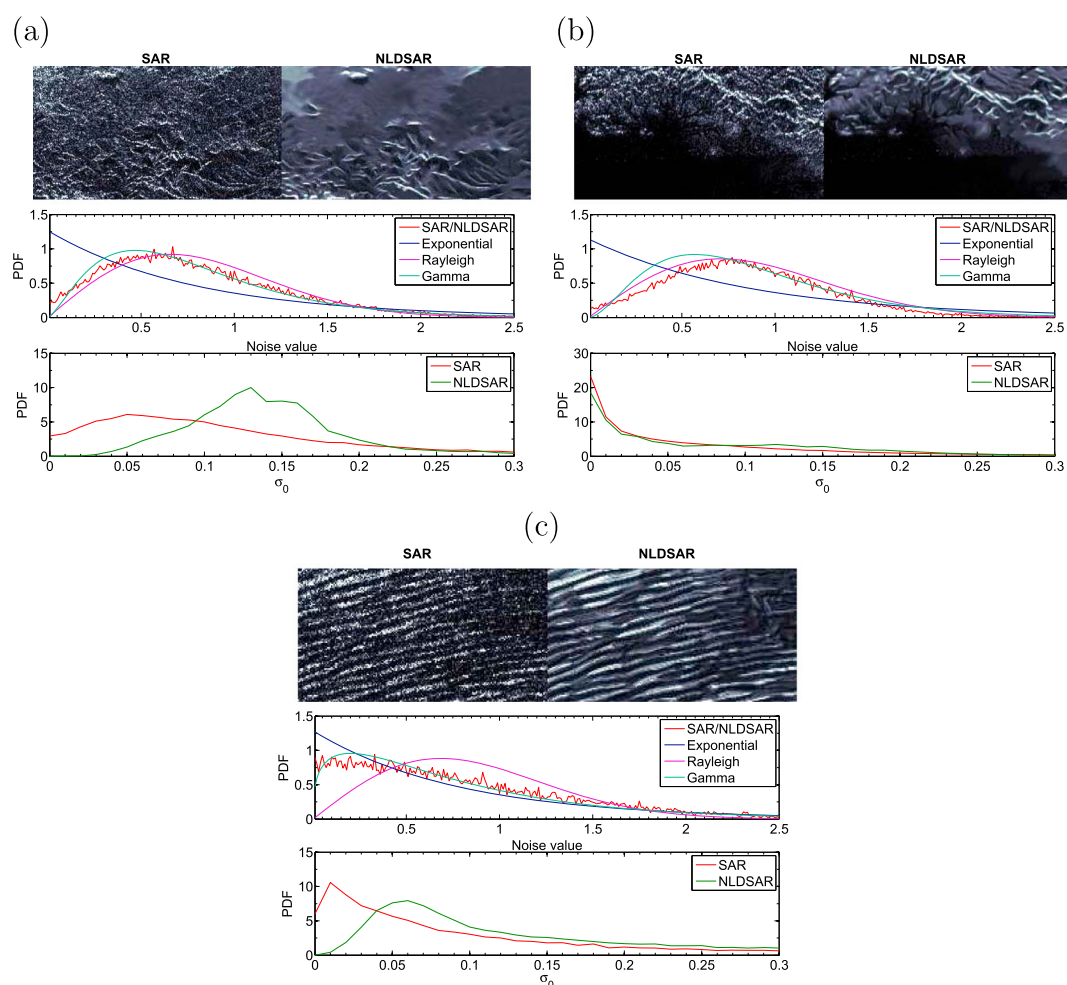
Figure 3. Examples of denoising at different regions, respectively, (a) Mayda Insula from T28, (b) Ligeia Mare from T28, and (c) Fensal dune field from T17. Top images show original SAR (left) and its NLDSAR counterparts (right). For each panel, middle graph shows distributions of removed noise (red curve) and the best fitted distribution, i.e., exponential, Rayleigh, and gamma, in dark blue, purple, and green, respectively. The bottom graphs show histograms of SAR and NLDSAR and illustrate how the multiplicative noise affects the backscatter distribution from place to place.

observation geometries show patches with matching geometric boundaries and relative brightness to neighboring patches (see Text S1).

This leads to the following understanding. Features that are covered by a small number of pixels may have brightness variations that are insufficiently resolved. In this case, the denoising process results in clustering the pixel values in artificially narrow ranges that may appear as pa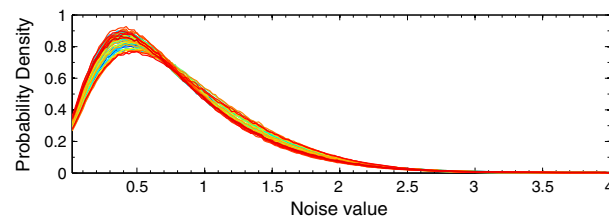tches. However, the boundaries of such synthetically generated patches vary with specific realizations of the noise and hence are not expected to align across multiple observations at differing geometries. Note that in all of our tests, the filtered result is at least slightly smoother than the input. That means there is no tendency to artificially sharpen up smooth variations in brightness into sharp-edged patches.

As described in Text S1, our tests show that although patchiness on a small scale can be introduced as an artifact in some cases, the
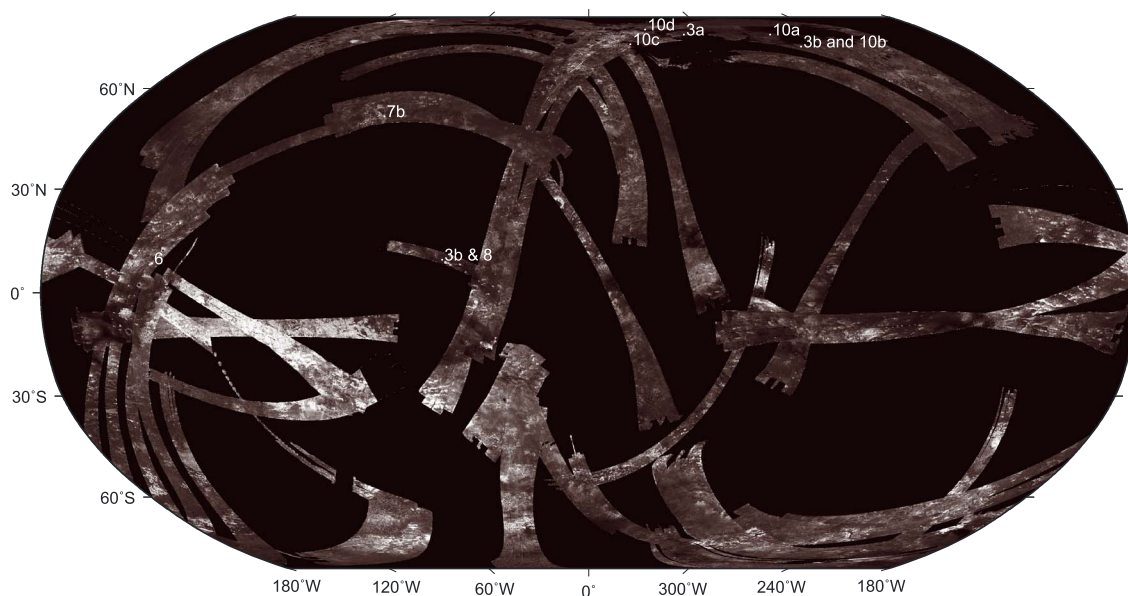

Figure 4. Histograms of removed noise over the complete T17 swath obtained with 50 sets of the parameters ($h^2 \in [1; 15]$, $T \in [1; 15]$, $t \in [1; 4]$, $|W| \in [11 \times 11; 41 \times 41]$, and $|\Delta| \in [5 \times 5; 11 \times 11]$, see equation (2)). The derived noise distribution is not affected by the parameters and show in this case a Rayleigh distribution.

Figure 5. Current state of NLDSAR processing. Summary map of denoised Titan passes including flybys from TA to T65. Symbols with number indicate the location of examples illustrated in the manuscript in the respective figure number.

large consistent patches on Titan appear to be a property of the surface (or subsurface). The origin of the features remains enigmatic. The persistence of patches in overlapping images acquired in varying geometries, their localized appearance, as well as synthetic tests, all support, but do not prove, a geologic origin of patches. If indeed the areas within patches share similar radiometric properties, a hypothesis that would account for the phenomenon is one of resurfacing events producing deposits which overlay each other. If cryovolcanic in nature, several factors could influence the radar backscatter of the deposits, including
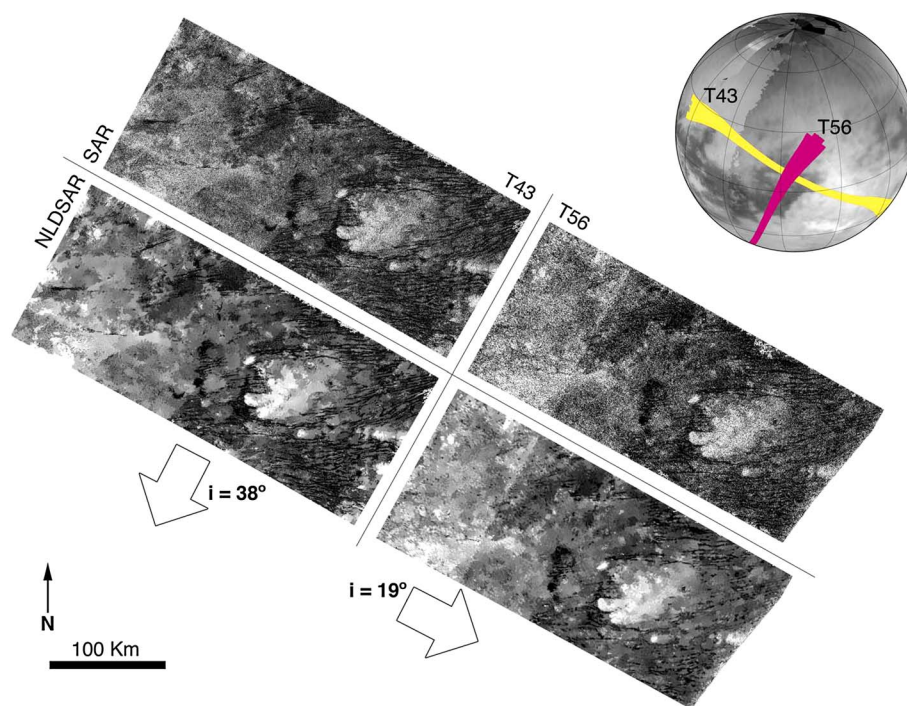

Figure 6. Overlap and observation geometry for T43 and T56 swaths over Tortula Facula (8°N, 144°W). The two swaths show orthogonal look directions (see outlines on Titan's sphere and white arrows directions) and different incidence angles **i** (see supporting information for additional analysis of this case).
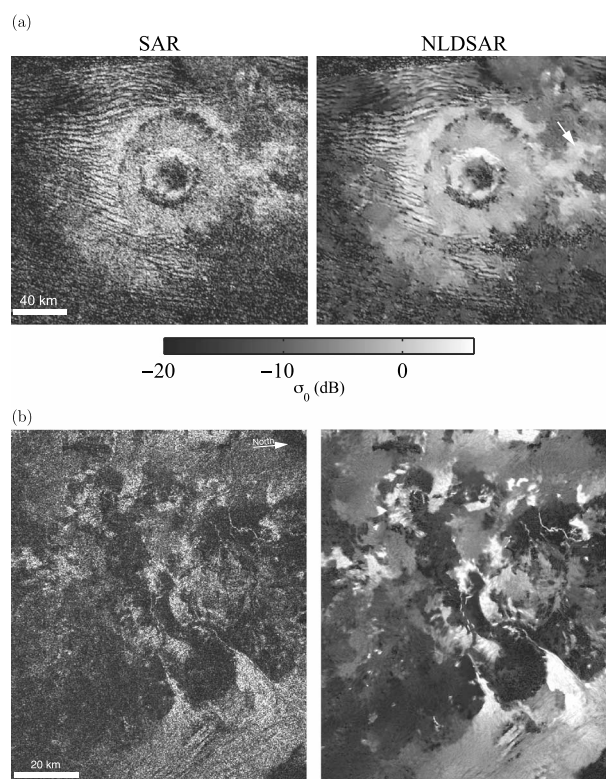
Figure 7. (a) NLDSAR image showing discreet surface structures near Momoy crater (11.6°N,44°W) observed in T77 (north is up). Ejecta blanket is indicated with the white arrow. (b) Leilah Fluctus (55°N,80°W) observed upon denoising on TA swath subset (north is indicated by the white arrow).

extrusion rate, cooling rate, or annealing; these may affect the backscatter values by surface roughness, or volume scattering. One example is shown in Figure 7a, where patches of uniform brightness and sharp boundaries may be interpreted as individual flows superimposed on one another. The ejecta blanket of Momoy crater may be interpreted as composed of individual flows sourced from the crater. Another potential origin of patches may be due to sedimentary processes as illustrated by Figure 7b, where possible alluvial cones are observed in association with fluvial channels.

Radar patchiness may also originate from subsurface structures due to regional variations in volume scattering [*Paillou et al.*, 2006], inherited from porosity or lithological structure. Liquid in the subsurface would alter the dielectric constant and may contribute to regional boundaries. Systematic mapping and analysis including incidence angle dependence is required in order to probe the origin of patches, but the low spatial resolution and limited areas of repeat coverage of the Cassini RADAR data hinders a definitive explanation.

3.2. Dunes

Extensive areas in Titan's equatorial region are covered by dunes [*Lorenz et al.*, 2006], with morphogenesis likely controlled by an atmospheric circulation trap at an altitude of 2 km [*Charnay and Lebonnois*, 2011; *Lorenz et al.*, 2010a]. We investigate the morphology of dunes in order to constrain such models. As shown in Figure 3, the dunes are more sharply defined with respect to interdune areas upon denoising. In speckled data the boundary between dune and interdune units is poorly defined and difficult to trace. In denoised images, dunes are seen to emerge from interdune regions with clear boundaries delineating the contact between the two units. Such clear boundaries do not appear on our synthetic tests as shown in Figures 1 and 2 (see also tests in Text S1). Cross section along the dune field shows that NLDSAR reveals a periodicity between dunes and interdunes (Figure 8). Due to this refinement, better morphometric estimates are possible: wavelength has been derived automatically from spectral estimation and we found $\lambda \simeq 3200$ m, in good agreement with previous manually measured estimations [*Radebaugh et al.*, 2008]. The denoised data enable enhanced dune morphogenesis analysis. *Ewing et al.* [2013] document the transition and evolution of extensive dunes to individual barchans and star dune forms. Large radar glints are isolated and highlighted in denoised data (Figures 3c and 8), enabling discrimination of their sources and refined estimates of the slopes. NLDSAR is useful for radarclinometry techniques as well as radargrammetry both providing elevation information, which in turn, enables the study of the interaction of dunes with the wind regime and the local topography [*Lucas et al.*, 2014].

3.3. Hydrology

Like Earth, Titan possesses an active hydrologic cycle with fluvial, lacustrine, and marine processes. While previous studies have identified geomorphic units involved in these processes [*Stofan et al.*, 2007; *Hayes et al.*, 2008; *Turtle et al.*, 2011], their interaction with the topography needs to be better understood. Recently, *Black et al.* [2012] studied the geometry of drainage networks and have shown numerically that fluvial incision has only modestly affected the topography, i.e., they found that fluvial networks reflect spatially averaged erosion of less than 9% of the initial topographic relief. We will show in this subsection how new insights into Titan's hydrology may be obtained from the processed NLDSAR data set.
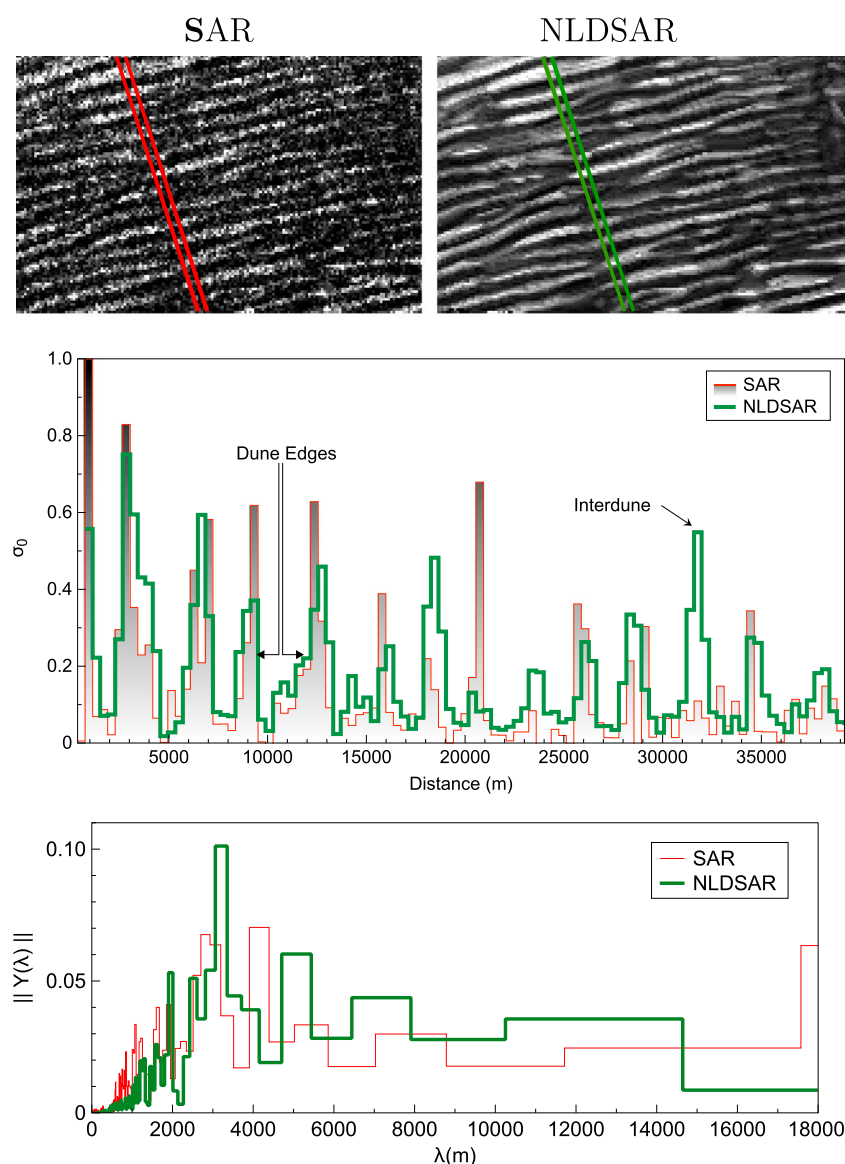
Figure 8. (top) T17 swath subset over a dunes field from SAR (left) and NLDSAR (right) data set. (middle) Red and green cross sections correspond to the profiles displayed below. Images on top show that dunes and interdunes are contiguous in NLDSAR images. (bottom) Profiles show that edges of dune/interdune in NLDSAR are consistent with those in SAR data. Figure 8 (bottom) shows the estimates of the power spectra along cross section for both SAR and NLDSAR data sets. The NLDSAR data provides a clear peak at a wavelength of 3200 m, whereas the unprocessed SAR data show a broad peak, actually two peaks, between 2500 m and 4500 m., because the speckle noise is not removed.

3.3.1. Valleys and Drainage Basins Morphology

The interest of NLDSAR image for hydrological analysis is illustrated on Figure 9, where bright channels are observed on T03 swath. The ratio between SAR and NLDSAR shows a randomly distributed noise which does not depend on the underlying brightness (Figure 9c). We show that features with widths of ~2 pixels are preserved in the NLDSAR image (highlighted by white arrows in Figures 9d and 9e), emphasizing the robustness of the denoising procedure. This example demonstrates the potential improvement for mapping fluvial features, and geological interpretations as discussed previously.

The objects and textures present in the NLDSAR image shown previously on Figure 9e correspond to recognizable features on the original noisy image (Figure 9d). For instance, linear patterns appearing in Figure 9e in the bright channel are interpreted to be part of the morphology as they follow the stream direction and are only present inside the valley. The presence of individual small channels inside a larger valley is
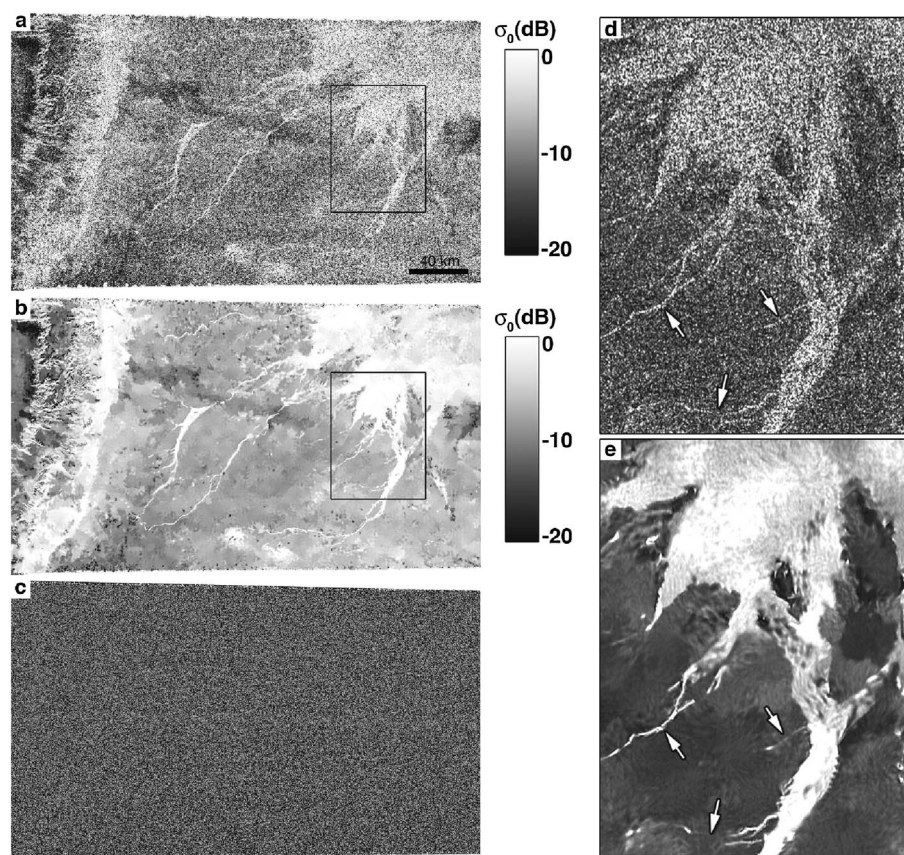
Figure 9. Example of denoising on T03 swath subset (20°N,80°W). (a) Original noisy SAR data and (b) denoised image, both in logarithmic contrast stretch. (c) The removed noise (i.e., ratio between the original noisy image and denoised image SAR/NLDSAR) showing no dependence on geologic features, contrast, edges, beam boundaries, or the initial value of SAR image. Black boxes in Figures 9a–9b indicate locations of magnified insets showing bright channels in the noisy image (Figure 9d) and the denoised image (Figure 9e). Both are displayed with a linear scale for a better contrast between bright channels and surrounding areas. White arrows indicate channels that are preserved and highlighted by the application of the denoising procedure. (North is up.)

similar to comparable rivers on Earth, where such a relationship indicates relatively high slopes, large sediment load with shallow streams of low sinuosity and a noncohesive bank material [*Schumm and Kahn*, 1972]. In this same area, patches of distinguishable brightness surround the channels (Figure 9e). The braided patterns here correlates with the transition between two patches, suggesting a possible difference in material properties of the substrate.

The shores of the northern seas have complex morphologies suggesting the action of fluvial processes that have sculpted the landscape in this region. Morphology is characterized by sea cliffs, spits, and bays as shown in Figures 10a and 10b. Whereas cliffs might be cut by waves (if waves are generated on Titan's seas, see discussions in *Lorenz et al.* [2010b, 2012] and *Hayes et al.* [2013a]), most of the morphologies observed are controlled by land processes. As mentioned previously, NLDSAR data set provides improvement of connectivity analysis and drainage integration estimation. Lake shorelines appear sharper (Figures 10a–10c).

Valleys morphologies attest to stream erosion along the shores (Figures 10a and 10b). Interestingly, some valleys incised at angles acute relative to the present shore of the Ligeia Mare and thus support the interpretation of temporal evolution (Figure 10b), where the lake level rose after the incision of the large fluvial valley. The valley is expected to form with drainage direction normal to past shoreline, which was modified upon flooding [*Aharonson et al.*, 2013; *Hayes et al.*, 2013b]. Jingpo Lacus shown in Figure 10c, exhibits valley features beneath a liquid cover, which appear even more clearly in NLDSAR data. These features indicate that rivers continue into the lake and eroded material is delivered further south. The presently submerged valleys indicate a rise in lake level subsequent to the significant erosion recorded by the river valley; given
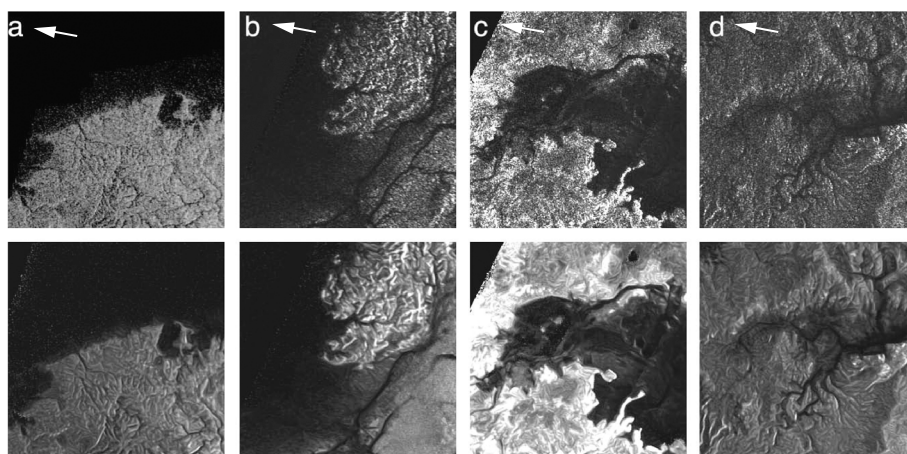
Figure 10. SAR images (top row) with their NLDSAR counterparts (bottom). North is toward the left. Each thumbnail is 112 km wide. Panels show (a) sea cliffs with spits and (b) bays, as well as (c) valleys incised at acute angles relative to the present shore of the Ligeia Mare. Channel forms within Jingpo Lacus show an increase width when the channel pass through lower radar values, suggesting southward flow direction beneath shallow liquid cover (Figure 10c) and NLDSAR data highlight variations in valley morphology (Figure 10d). Several knickpoints are identified at the valley head. (North is indicated by the white arrows.)

Figure 11. Digital elevation model of North Pole Region obtained from T25 and T28 denoised swaths. (a) 200 m contours ranging from −1000 to 200 m overlaying the T28 NLDSAR image scaled in dB. (b) Colorized topography and shaded relief map of the same area. Dark areas (when $\sigma_0 < -15$ dB) have been masked. SARTopo data have been overlayed on the DEM.

Figure 12. Stereo topography extracted over Mayda Insula using swaths T25 and T28 (79°N,48°E). (a) Correlation map obtained with SAR i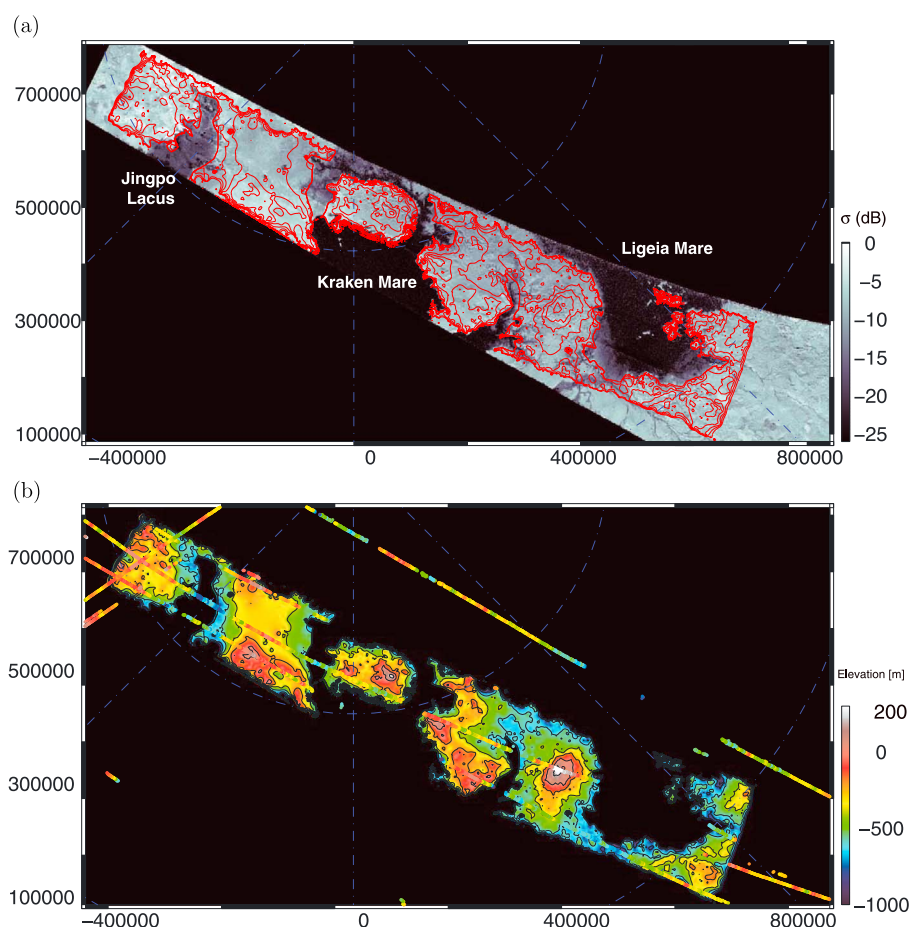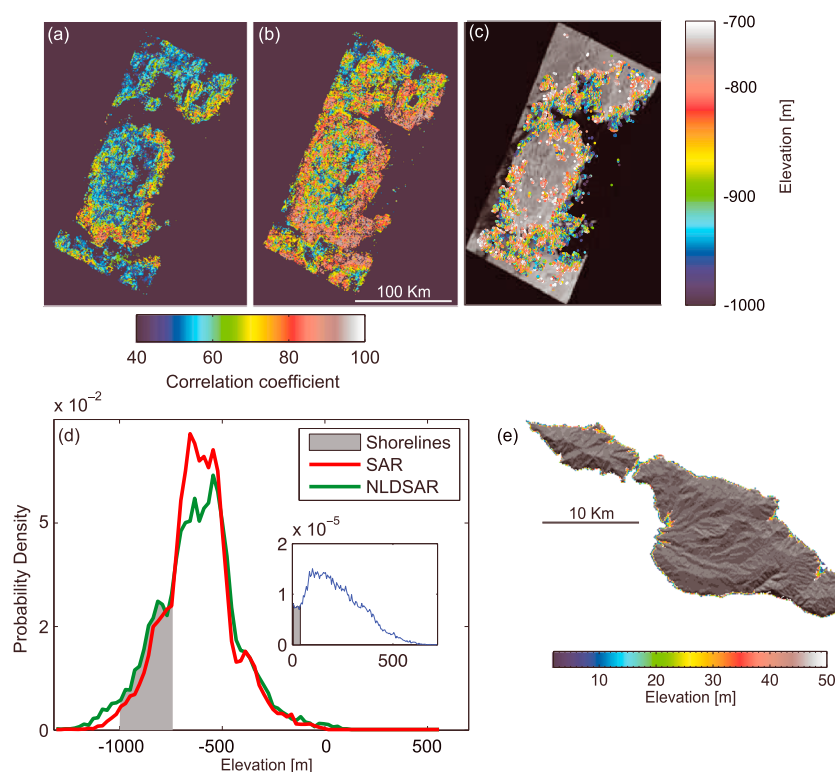mages; (b) Correlation map obtained with NLDSAR images; (c) Elevation corresponding to the gray area in the distribution of elevations shown in panel (d); (d) Hypsograms of extracted DEMs showing a bench in the distribution (gray area). Insert shows elevation hypsogram of Catalina Island, California with an analogous bench feature (gray area); (e) Catalina Island, CA shaded relief and elevations corresponding to the bench (gray area) in the distribution shown in inset of panel (d).

the relative densities of the material involved, submarine erosion of the channel is highly unlikely but is not ruled out.

NLDSAR data highlight variations in valley morphology and SAR backscatter, suggesting a break in slope in the valley incision. Figure 10d shows an example of an eroded valley, fed by a smaller channel. The transition from the narrower, low-contrast valley to the broader, more distinct portion is sharp and indicates a discontinuity. The presence of knickpoints (i.e., location of a river where a sharp change in the topography slope occurs) may indicate either lithological stratification, erosion mechanism, or disequilibrium response of the topography to runoff events [*Lamb et al.*, 2007].

3.3.2. Topographic Analysis

We derived a digital elevation model (DEM) from radargrammetry based on the sensor model previously developed [*Kirk et al.*, 2007] and the use of the commercial photogrammetry software SOCET SET (Figure 11). We used a pair of original SAR images, as well as NLDSAR images, allowing a significant enhancement in the edges of structures and thus facilitating the correlation needed for topographic extraction. Using NLD-SAR data, we obtained a greater number of matching points (up to 80%) and a better correlation (59% of the pixels give a good correlation in the denoised data compared with 18% in the original SAR image). The accuracy of stereo matching is controlled by the correlation function computed by the stereo matching algorithm from the pair of images. The denoised data result in a higher minimum curvature of the correlation function, with sharper peaks in the correlation, leading to more precise measurements. Linear error of 90% is commonly used for evaluating DEMs and is defined as the error in elevation of one point with respect to another point within the DEM at 90% probability. Along the shorelines, we obtained values of this error measure below 80 m, a level which was unattainable previously as the best values from the nondenoised data are greater than 180 m at the same location (i.e., same parallax and height geometry). This denser and
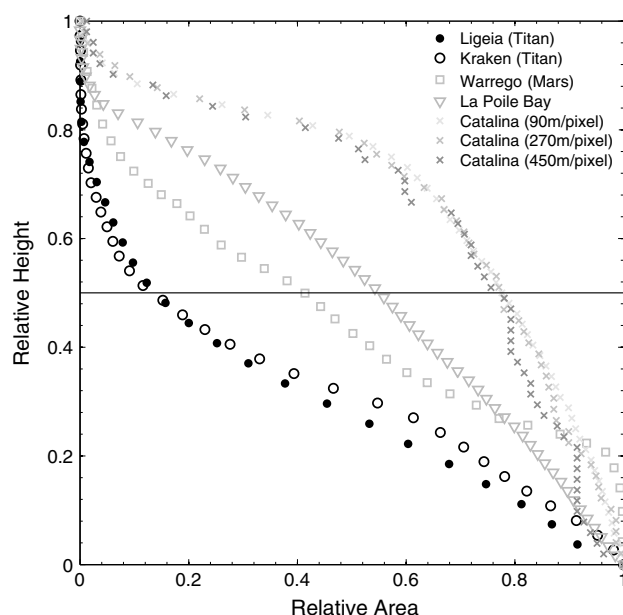
Figure 13. Hypsometry of drainage basins on Earth, Mars, and Titan. Kraken and Ligeia are drainage basin selected around these seas. Warrego Vallis is an example on Mars (after *Ansan and Mangold* [2006]). Terrestrial examples have been obtained from Shuttle Radar Topography Mission (SRTM) data set. For Catalina, different resolutions obtained by reducing the pixel size using a nearest-neighbor interpolation are shown for comparison.

more accurate elevation extraction leads to a finer analysis of the shorelines of the northern seas. The elevation ranges from −1000 to 400 m with respect to Titan's geoid [i.e., see *less et al.*, 2010] in agreement with SARTopo [*Kirk et al.*, 2007; *Stiles et al.*, 2009; *Lorenz et al.*, 2013] as shown on Figure 11b.

Several observations are of note on the basis of the derived topography. The shorelines of Ligeia Mare and Kraken Mare are located at similar altitudes (i.e., within 90 m) compared with uncertainties in the DEM which are ∼80 m along the shores (see contour lines on Figure 11a). A large hill located between Ligeia and Kraken Mare appears to control the radial pattern of valleys. While the resolution of the data does not allow measurement of the slope of the channel floor, these valleys incised surfaces whose slopes vary between 1×10^{-4} and 0.02.

A histogram of elevations allows the identification of a shoulder in the distribution, suggesting that fluvial and/or lacustrine processes have affected the terrain, creating a topographic bench (Figure 12). Similar patterns are commonly seen in the near-shore topography distribution on Earth (Figures 12d and 12e). These results are consistent with observations from SAR images (i.e., presence of valleys near the shores, see Figure 10a) and show that here erosion and sediment transport may affect the topography substantially, that their integrated action is quantified volumetrically. By spatially integrating this topography, an estimation of ∼1 m of removed material is measured along Mayda Insula shorelines. This is consistent with values obtained recently by *Black et al.* [2012] (Figure 12). The evidence supporting topographic adjustment to erosion and sediment transport in some near-shore locations, contrasts with a disequilibrium response recorded by knickpoints previously described and valley geometries. Taken together, these observations indicate late stage erosion and modification of Titan's topography, with recent events superimposed on a more mature, fluvially modified landscape.

Comparison of hypsometric curves (*i.e.*, frequency distribution of elevations) of drainage basin on Titan around the northern seas with terrestrial and Martian examples suggest a late stage of erosion [*Ansan and Mangold*, 2006] (Figure 13). Hypsometry of drainage basin around Northern Seas suggests that these networks are mature. This is in good agreement with broad and low valleys visible on SAR images. On the other hand, knickpoints mentioned previously might be adjustments to 'recent' level raise regarding the timescale of processes. Beyond the DEM resolution, knickpoints can be formed at a shorter timescale compared to the equilibrium timescale of the drainage basin.

Dark seas and lakes exhibit extremely low and homogeneous RADAR returns, which mark an absorptive and smooth surface at the RADAR wavelength. They are commonly considered to be covered by liquid hydrocarbons [*Stofan et al.*, 2007; *Brown et al.*, 2008; *Paillou et al.*, 2008]. More recently, *Cornet et al.* [2012a] have suggested that RADAR brighter areas within Ontario Lacus correspond to mudflats as opposed to be completely covered by a standing liquid body, by analogy to the Etosha lake in Namibia. It is difficult to distinguish between these two hypotheses when only comparing backscatter values, which heavily rely on the unknown parameters such as the scattering properties of the surface and the complex dielectric properties of the liquid. As such, only areas that are consistently below the radar's noise floor can reliably be interpreted
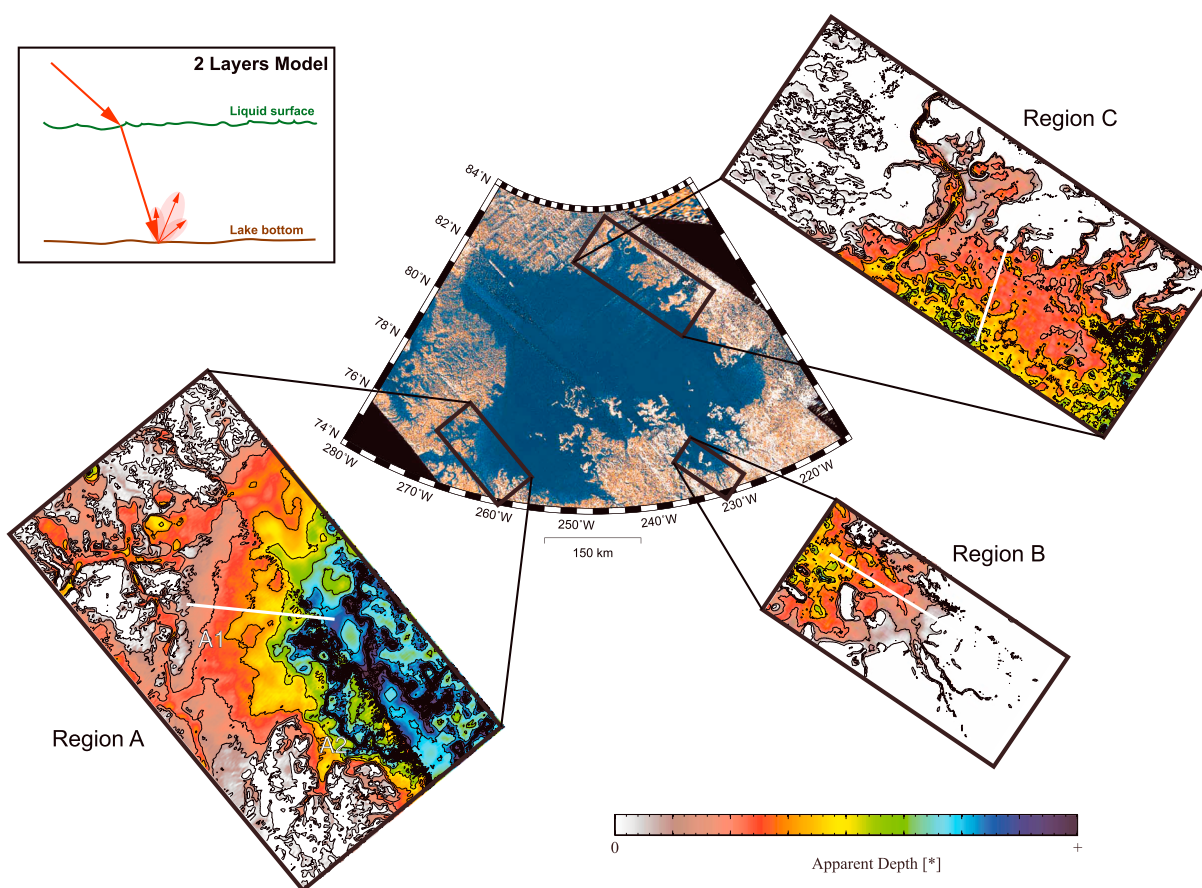
Figure 14. Bathymetry maps of near-shore regions of Ligeia Mare from NLDSAR. Radar backscatter values were converted to apparent depth (i.e., depth/loss tangent) using a two-layer model of radar energy penetration in the liquid [*Hayes et al.*, 2010] as depicted in the inset schematic. Straight lines in white indicates the bathymetry profiles location of Figure 15 for Regions A–C, respectively.

as liquid bodies (in the absence of centimeter-smooth solid surface) [*Paillou et al.*, 2008]. The NLDSAR might potentially help in visualizing the heterogeneities within the mares and lakes areas.

The DEM we obtained over the North polar seas constrains the elevation of liquid bodies. In Figure 11a we show that the dark areas of Kraken Mare and Ligeia Mare lie at about −1000 m, also seen in the hypsograms in Figure 12d. The denoised images and DEM (Figure 11) further indicate that slopes leading into Ligeia Mare are at an elevation that is below this shoreline level and hence likely covered by a shallow liquid body (i.e., few meters). We employ denoised images in order to extract bathymetry based on a two-layer model proposed by *Hayes et al.* [2010], accounting for the reflection and transmission of radar energy at the air interface and through the liquid medium (Figure 14). The NLDSAR image enables obtaining a bathymetry map of large seas with the noise optimally removed, and no local binning (as was performed by *Hayes et al.* [2010] and *Wye et al.* [2010]).

Because the subsurface scatter is not necessary uniform, absolute depths cannot be obtained. Assuming zero backscatter form the surface, we report here the ratio of depth/loss tangent as an "apparent" bathymetric depth (Figure 14). Our results suggest the presence of submerged valleys beneath a shallow hydrocarbons layer. Portions of valleys currently submerged exhibit similar widths and network morphology to portions exposed, supporting the formation of the submerged valleys prior to flooding (Figure 14).

The timing of the putative flooding event is poorly constrained with limited observations; the possibilities range from a catastrophic event after the initial channel formation and shoreline establishment, to periodic, or continuous. Surface process durations and ages are currently uncertain on Titan with the available data.
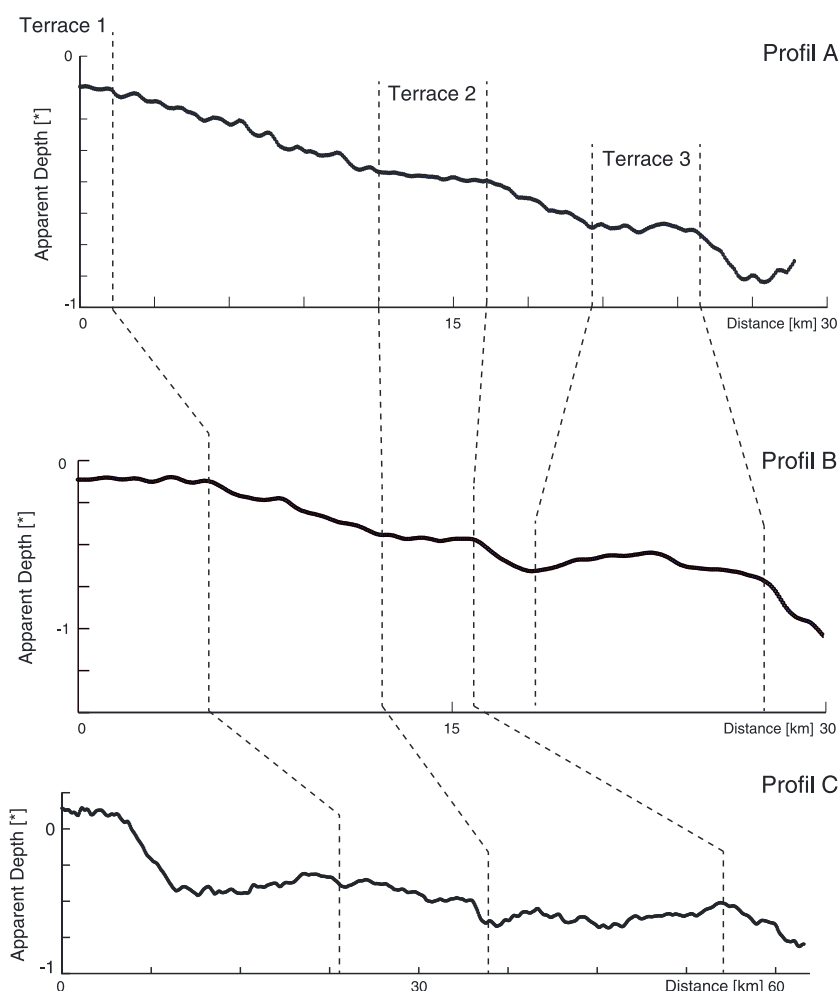
Figure 15. Terraces show similar apparent depths (i.e., depth/loss tangent) from two different swaths (T28 and T29) suggesting change in base level of Ligeia Mare. Values are reported for comparison among profiles and should not be interpreted as absolute depths. Location of profiles are indicated in Figure 14.

Several features indicate shoreline benches in portions of the lake. Channels terminate at similar depths at distant locations around the lake, indicating adjustment of the fluvial system to a common base level, lower than the present liquid level. Apparent bathymetric profiles further indicate benches, as a significant break in slope exists between profiles in region A1 and region A2 (Figure 14). The shallow slopes in region A1 allowed the lake to flood over a large lateral extent (~14 km).

In addition, benches in bathymetry are observed in regions A and C at similar "apparent" liquid depths (Figure 15). The bottom depth of the valley in region C is also near the same benches, suggesting that these valleys are equilibrated with the deeper marine bench. Assuming the latter is the base level of the lake during the formation of the valley provides an upper bound on $\delta h/h \sim 0.25$ (where h is the maximum depth of the lake, recent estimation of h give ~150 m [*Mastrogiueppe et al.*, 2014]). Note, the relative volumetric change may be larger, since, for example, for a constant shore slope the relative volumetric change $\delta v/v$ scales as $3(\delta h/h)$.

Taken together, these observations provide evidence that the landscape in this area has been developed by stream erosion, with subsequent rise of lake level swamping the river valleys. These liquid level increases may be compared with lake recession observed in the south. Ontario Lacus was seen to change over several years of observations, from imaging science subsystem/SAR comparison [*Hayes et al.*, 2011; *Turtle et al.*, 2011] at a rate of several tens of cm/yr. Potential past high stands of the lake were also mapped by *Barnes et al.* [2009] using VIMS images. Overall, the observed changes correspond to a lake recession comparable in

areal extent to the increases deduced here in the north but could act at very different timescales. However, this possible change level of Ontario is still an open question as alternative analysis suggest no change by comparing 2005 and 2010 SAR observations [*Cornet et al.*, 2012b].

The liquid level increases in the north evident in the morphology and bathymetry may be due to changes on seasonal or longer timescales. Several meters of change are predicted from GCMs to occur due to seasonal cycles [*Mitchell*, 2008; *Schneider et al.*, 2012]; larger changes, or order tens of meters, are expected from orbital oscillations on timescale of tens to hundreds of kiloyears [*Aharonson et al.*, 2009; *Schneider et al.*, 2012].

The interpreted rise in liquid level could also result, or partially result, from subsidence of the basin due to surface loading [*Choukroun and Sotin*, 2012]. The amplitude of subsidence depends on the densities and other parameters. But an estimate may be obtained if for example, at an assumed depth of isostatic compensation, the additional load of liquid methane of density $\rho_{\text{load}} = 422$ kg/m^3 is balanced by a deflection of the lighter icy crust into a denser medium of water of density $\rho_{\text{lm}} = 1000$ kg/m^3. The resulting subsidence in response to a load of height h will be $\delta h = (\rho_{\text{load}}/\rho_{\text{m}})h$, that is approximately 42 m for every 100 m of liquid added to the surface. These values are consistent with our observations but cannot be determined directly from the data without additional knowledge of the subsurface structure. Derivation of the subsurface backscatter function is hence necessary for quantifying the elevation magnitude of these base-level changes.

4. Conclusions

We show in this study that nonlocal denoising technique can be applied to Cassini SAR data in order to improve the use of these images both in qualitative interpretation and in quantitative analysis. The new NLDSAR data set, with a significantly reduced speckle noise, clarifies geologic relations. We highlight and interpret morphology associated with hydrologic processes: flooded valleys, knickpoints, evidence for runoff associated with empty isolated lakes, and benches within Ligeia Mare.

Analysis of the denoising procedure and SAR images of Titan provides several new insights. It enables retrieval of the noise distribution without prior information. The noise distribution differs from region to region on Titan and could depend on the underlying reflectivity, roughness properties, and number of looks, which vary along the swaths. We observed unusual patches in the denoised images. Their origin remains enigmatic. One possible interpretation is that overlapping deposits from cryovolcanic resurfacing events of various ages cause discreetly varying properties that translate to radar surface brightness. Data processing artifacts are unlikely to result in the observed persistent patches over varying geometries and are hence disfavored, though not ruled out completely. The comparison between original data (SAR) and denoised data (NLDSAR) shows that the structures are preserved by the numerical process and at most, only small biases are introduced. This is particularly well illustrated in the dune field, for which we obtain a similar wavelength in power spectral analysis of the denoised images compared to manual measurements in the original images. The enhanced images enable us to more easily identify, map, and interpret various fluvial and lacustrine morphologies. We show a significant improvement in DEM generation by using the NLDSAR data, offering a refinement in topographic analysis. This study offers new evidence for base-level elevation changes in northern seas but cannot be compared directly with lake recession observed in the south [*Hayes et al.*, 2011; *Turtle et al.*, 2011] as the two may be acting over significantly different timescales: while several meters as associated with seasonal cycles, tens of meters, are expected from orbital oscillations on timescales of tens to hundreds of kiloyears. As discussed, rise in liquid level could also partially result from subsidence of the basin. These results are consistent with observations from SAR images and show that erosion and sediment transport have affected the topography substantially and that their integrated action could be quantified volumetrically.

References

Aharonson, O., A. G. Hayes, J. I. Lunine, R. D. Lorenz, M. D. Allison, and C. Elachi (2009), An asymmetric distribution of lakes on Titan as a possible consequence of orbital forcing, *Nat. Geosci.*, **2**, 851–854.

Aharonson, O., A. Hayes, R. Lopes, A Lucas, P. Hayne, and J. T. Perron (2013), Titan's surface geology, in *Titan: Surface, Atmosphere and Magnetosphere*, edited by C. G. Mueller-Wodarg, T. Cravens, and E. Lellouch, Cambridge Univ. Press, Cambridge, U. K.

Ansan, V., and N. Mangold (2006), New observations of Warrego Valles, Mars: Evidence for precipitation and surface runoff, *Planet. Space Sci.*, **54**, 219–242.

April, G. V., and E. R. Harvy (1991), Speckle statistics in four-look synthetic aperture radar imagery, *Opt. Eng.*, *30*(4), 375–381.

Barnes, J. W., et al. (2009), Shoreline features of Titan's Ontario Lacus from Cassini/VIMS observations, *Icarus*, *201*, 217–225.

Black, B. A., J. T. Perron, S. A. Drummond, and D. M. Burr (2012), Estimating erosional exhumation on Titan from drainage network morphology, *J. Geophys. Res.*, *117*, E08006, doi:10.1029/2012JE004085.

Brown, R. H., L. A. Soderblom, J. M. Soderblom, R. N. Clark, R. Jaumann, J. W. Barnes, C. Sotin, B. Buratti, K. H. Baines, and P. D. Nicholson (2008), The identification of liquid ethane in Titan's Ontario Lacus, *Nature*, *454*, 607–610.

Buades, A., B. Coll, and J.-M. Morel (2005), A non-local algorithm for image denoising, in *Proceeding CVPR '05 Proceedings of the 2005 IEEE Computer Society Conference on Computer Vision and Pattern Recognition (CVPR'05)*, vol. 2, pp. 60–65, IEEE Computer Soc., Washington, D. C.

Burr, D., et al. (2012), Fluvial features on Titan: Insights from morphology and modeling, *Geol. Soc. Am. Bull.*, *3–4*, 299–321.

Charnay, B., and S. Lebonnois (2011), Titan's lower troposphere: Thermal structure and dynamics, Abstracts P33E-1791 paper presented at 2011 Fall Meeting, AGU, San Francisco, Calif., 13-17 Dec.

Choukroun, M., and C. Sotin (2012), Is Titan's shape caused by its meteorology and carbon cycle?, *Geophys. Res. Lett.*, *39*, L04201, doi:10.1029/2011GL050747.

Cornet, T., et al. (2012a), Geomorphological significance of Ontario Lacus on Titan: Integrated interpretation of Cassini VIMS, ISS and RADAR data and comparison with the Etosha Pan (Namibia), *Icarus*, *218*, 788–806.

Cornet, T., et al. (2012b), Edge detection applied to Cassini images reveals no measurable displacement of Ontario Lacus' margin between 2005 and 2010, *J. Geophys. Res.*, *117*, E07005, doi:10.1029/2012JE004073.

Deledalle, C.-A., L. Denis, and F. Tupin (2009), Iterative weighted maximum likelihood denoising with probabilistic patch-based weights, *IEEE Trans. Image Process.*, *18*(12), 2661–2672.

Elachi, C., et al. (2005), Cassini radar views the surface of Titan, *Science*, *308*, 970–974.

Ewing, R. C., A. G. Hayes, and A. Lucas (2013), *Reorientation Time-Scales of Titan's Equatorial Dunes,* 44th Lunar and Planetary Science Conference.

Frost, V. S., J. A. Stiles, K. S. Shanmugan, and J. Holtzman (1982), A model for radar images and its application to adaptive digital filtering of multiplicative noise, *IEEE Trans. Pattern Anal. Mach. Intell.*, *2*, 157–166.

Goodman, J. (1976), Some fundamental properties of speckle, *J. Opt. Soc. Am.*, *66*(11), 1145–1150.

Hayes, A. G., et al. (2008), Hydrocarbon lakes on Titan: Distribution and interaction with a porous regolith, *Geophys. Res. Lett.*, *35*, L09204, doi:10.1029/2008GL033409.

Hayes, A. G., et al. (2010), Bathymetry and absorptivity of Titan's Ontario Lacus, *J. Geophys. Res.*, *115*, E09009, doi:10.1029/2009JE003557.

Hayes, A. G., et al. (2013a), Wind driven capillary-gravity waves on Titan's lakes: Hard to detect or non-existent?, *Icarus*, *225*, 403–412.

Hayes, A. G., W. E. Dietrich, R. L. Kirk, E. P. Turtle, J. W. Barnes, A. Lucas, O. Aharonson, and K. L. Mitchell (2013b), *Morphologic Analysis of Polar Landscape Evolution on Titan,* 44th Lunar and Planetary Science Conference.

Hayes, A. G. O., et al. (2011), Transient surface liquid in Titan's polar regions from Cassini, *Icarus*, *211*(1), 655–671.

Hervet, E., R. Fjrtfort, P. Marthon, and A. Lopes (1998), Comparison of wavelet based and statistical speckle filters, in *SPIE: EUROPTO Conference on SAR Analysis, Modeling, and Techniques, Society of Photo-Optical Instrumentation Engineers, September 1998, Barcelona, Spain*, pp. 1–12, doi:10.1117/12.331361.

Iess, L., N. Rappaport, R. A. Jacobson, P. Racioppa, D. J. Stevenson, P. Tortora, J. W. Armstrong, and S. W. Asmar (2010), Gravity field, shape, and moment of inertia of Titan, *Science*, *327*, 1367–1369.

Kirk, R. L., E. Howington-Kraus, K. L. Mitchell, S. Hensley, B. W. Stiles, and Cassini RADAR Team (2007), *First Stereoscopic Radar Images of Titan,* Lunar and Planetary Institute Science Conference Abstracts.

Kocurek, G., and R. C. Ewing (2005), Aeolian dune field self-organization—Implications for the formation of simple versus complex dune field patterns, *Geomorphology*, *72*, 94–105.

Lamb, M. P., A. D. Howard, W. E. Dietrich, and J. T. Perron (2007), Formation of amphitheater-headed valleys by waterfall erosion after large-scale slumping on Hawaii, *Geol. Soc. Am. Bull.*, *119*(7–8), 805–822.

Langhans, M. H., et al. (2011), Titan's fluvial valleys: Morphology distribution, and spectral properties, *Planet. Space Sci.*, *60*, 34–51.

Lee, J. S. (1981), Refined filtering of image noise using local statistics, *Comput. Graphics Image Process.*, *15*(4), 380–389.

Lee, J.-S. (1986), Speckle suppression and analysis for synthetic aperture radar images, *Opt. Eng.*, *25*(5), 636–643.

Lorenz, R. D., et al. (2006), The sand seas of Titan: Cassini RADAR observations of 574 longitudinal dunes, *Science*, *312*, 724–727.

Lorenz, R. D., et al. (2008), Fluvial channels on Titan: Initial Cassini RADAR observations, *Planet. Space Sci.*, *56*, 1132–1144.

Lorenz, R. D., P. Claudin, B. Andreotti, J. Radebaugh, and T. Tokano (2010a), A 3 km atmospheric boundary layer on Titan indicated by dune spacing and Huygens data, *Icarus*, *205*, 719–721.

Lorenz, R. D., C. Newman, and J. I. Lunine (2010b), Threshold of wave generation on Titan's lakes and seas: Effect of viscosity and implications for Cassini observations, *Icarus*, *207*, 932–937.

Lorenz, R. D., T. Tokano, and C. E. Newman (2012), Winds and tides of Ligeia Mare, with application to the drift of the proposed time TiME (Titan Mare Explorer) capsule, *Planet. Space Sci.*, *60*, 72–85.

Lorenz, R. D., et al. (2013), A global topographic map of Titan, *Icarus*, *225*, 367–377.

Lucas, A., et al. (2014), Growth mechanisms and dune orientation on Titan, *Geophys. Res. Lett.*, *41*, doi:10.1002/2014GL060971, in press.

Mastrogiueppe, M., et al. (2014), The bathymetry of a Titan sea, *Geophys. Res. Lett.*, *41*, 1432–1437, doi:10.1002/2013GL058618.

Mitchell, J. L. (2008), The drying of Titan's dunes: Titan's methane hydrology and its impact on atmospheric circulation, *J. Geophys. Res.*, *113*, E08015, doi:10.1029/2007JE003017.

Paillou, P., M. Crapeau, C. Elachi, S. Wall, and P. Encrenaz (2006), Models of SAR backscattering for bright flows and dark spots on Titan, *J. Geophys. Res.*, *111*, E11011, doi:10.1029/2006JE002724.

Paillou, P., K. Mitchell, S. Wall, G. Ruffie, C. Wood, R. Lorenz, E. Stofan, J. Lunine, R. Lopes, and P. Encrenaz (2008), Microwave dielectric constant of liquid hydrocarbons: Application to the depth estimation of Titan's lakes, *Geophys. Res. Lett.*, *35*, L05202, doi:10.1029/2007GL032515.

Polzehl, J., and V. Spokoiny (2006), Propagation-separation approach for local likelihood estimation, *Probab. Theory Rel.*, *135*(3), 335–362.

Radebaugh, J., R. Lorenz, S. Wall, J. Lunine, R. Kirk, R. Lopes, F. Paganelli, E. Stofan, and The Cassini Radar Team (2008), Dunes on Titan from Cassini RADAR, *Icarus*, *194*, 690–703.

Schulze, M. A., and Q. X. Wu (1995), Noise Reduction in synthetic aperture radar imagery using a morphology-based nonlinear filter, in *Proceedings of DICTA 95, Digital Image Computing: Techniques and Applications, 6-8 December, 1995, Brisbane, Australia*, pp. 661–666. [Available at http://citeseerx.ist.psu.edu/viewdoc/summary?doi=10.1.1.17.4636.]

Schneider, T., S. D. Graves, E. L. Schaller, and M. E. Brown (2012), Polar methane accumulation and rain storms on titan from simulations of the methane cycle, *Nature*, *481*, 58–61.

Schumm, S. A., and H. R. Kahn (1972), Experimental study of channel patterns, *Bull. Geol. Soc. Am.*, *83*, 1755–1770.

Stiles, B., et al. (2009), Determining Titan surface topography from Cassini SAR data, *Icarus*, *202*(2), 584–598.

Sotin, C., et al. (2005), Release of volatiles from a possible cryovolcano from near-infrared imaging of Titan, *Nature*, *435*, 786–789.

Stofan, E. R., et al. (2006), Mapping of Titan: Results from the first Titan radar passes, *Icarus*, *185*, 443–456.

Stofan, E. R., et al. (2007), The lakes of Titan, *Nature*, *445*, 61–64.

Turtle, E. P., et al. (2011), Rapid and extensive surface changes near Titan's equator: Evidence of april showers, *Science*, *331*(6023), 1414–1417.

Wye, L. C., et al. (2010), Constraining depths and wave heights for Titan's lakes with Cassini radar data, paper presented at 2010 Fall Meeting, AGU.